Journal of the Mechanics and Physics of Solids 102 (2017) 224–238

Contents lists available at ScienceDirect

Journal of the Mechanics and Physics of Solids

journal homepage: www.elsevier.com/locate/jmps

Bio-inspired "jigsaw"-like interlocking sutures: Modeling, optimization, 3D printing and testing

I.A. Malik, M. Mirkhalaf, F. Barthelat*

Department of Mechanical Engineering, McGill University, 817 Sherbrooke Street West, Montreal, QC H3A 2K6, Canada

ARTICLE INFO

Article history:
Received 3 November 2016
Revised 29 January 2017
Accepted 2 March 2017
Available online 3 March 2017

Keywords:
Suture
Analytical model
Finite element simulation
Optimization
3D printing

ABSTRACT

Structural biological materials such as bone, teeth or mollusk shells draw their remarkable performance from a sophisticated interplay of architectures and weak interfaces. Pushed to the extreme, this concept leads to sutured materials, which contain thin lines with complex geometries. Sutured materials are prominent in nature, and have recently served as bioinspiration for toughened ceramics and glasses. Sutures can generate large deformations, toughness and damping in otherwise all brittle systems and materials. In this study we examine the design and optimization of sutures with a jigsaw puzzle-like geometry, focusing on the non-linear traction behavior generated by the frictional pullout of the jigsaw tabs. We present analytical models which accurately predict the entire pullout response. Pullout strength and energy absorption increase with higher interlocking angles and for higher coefficients of friction, but the associated high stresses in the solid may fracture the tabs. Systematic optimization reveals a counter-intuitive result: the best pullout performance is achieved with interfaces with low coefficient of friction and high interlocking angle. We finally use 3D printing and mechanical testing to verify the accuracy of the models and of the optimization. The models and guidelines we present here can be extended to other types of geometries and sutured materials subjected to other loading/boundary conditions. The nonlinear responses of sutures are particularly attractive to augment the properties and functionalities of inherently brittle materials such as ceramics and glasses.

1. Introduction

Natural hard materials such as bone (Koester et al., 2008; Currey, 2002), tooth enamel (Bajaj et al., 2010), sea shells (Barthelat et al., 2007), or turtle carapace (Chen et al., 2015) display unique and attractive combinations of strength, toughness, deformability and puncture resistance, properties that are difficult to combine in engineering materials (Ritchie, 2011). This outstanding performance is possible by their internal architectures, which can be described as assemblies of stiff and strong building blocks (collagen or chitin fibers, mineral tablets) (Barthelat, 2015) bonded by weaker interfaces. These interfaces are as important as the building blocks and fulfill critical structural functions (Barthelat et al., 2016): They deflect and channel cracks into toughening configurations (He et al., 1994; Khayer Dastjerdi et al., 2013), they enable large deformations (Smith et al., 1999) and they provide deformation hardening to spread energy dissipative mechanisms throughout large volumes of the materials (Barthelat, 2015; Barthelat et al., 2016; Dunlop et al., 2011; Fratzl et al., 2004; Fratzl et al., 2016; Meyers et al., 2008). The mechanical behavior of these interfaces is typically nonlinear and governed by friction or

* Corresponding author.
E-mail address: francois.barthelat@mcgill.ca (F. Barthelat).

http://dx.doi.org/10.1016/j.jmps.2017.03.003
0022-5096/

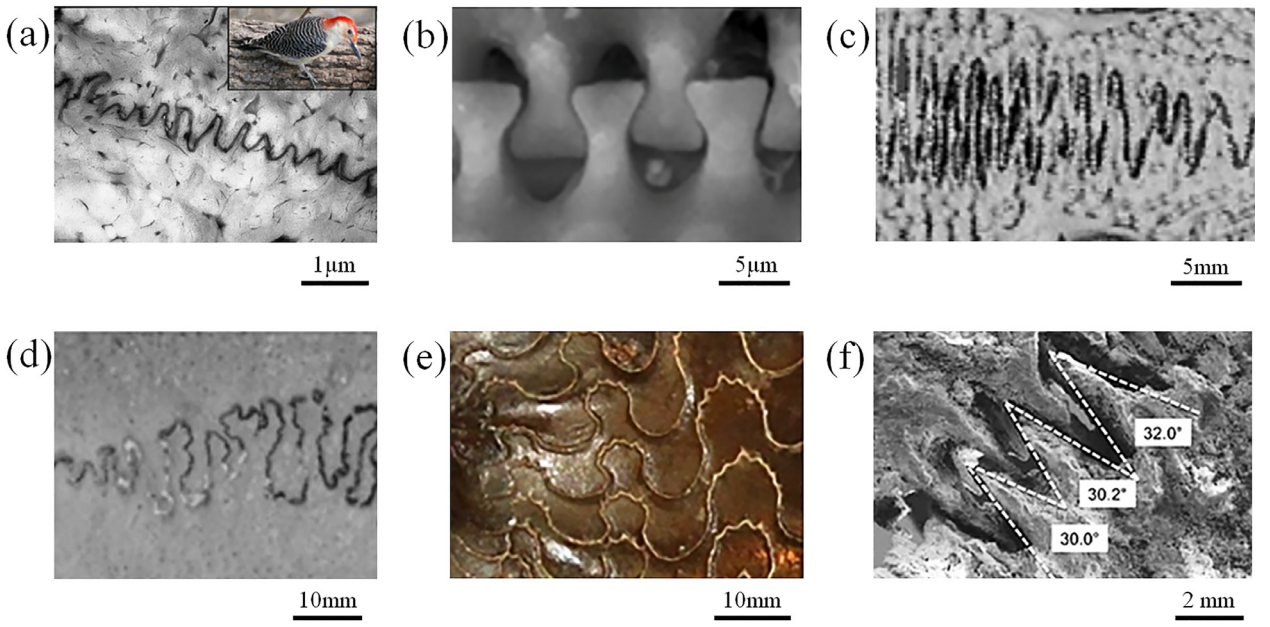

Fig. 1. Examples of sutured interfaces in nature: (a) red-bellied woodpecker (Melanerpes carolinus) beak (adapted from Lee et al., 2014), (b) linking girdles of diatoms (adapted from Lin et al., 2014), (c) marine threespine stickleback (Gasterosteus aculeatus) (adapted from Song et al., 2010), (d) Pan troglodytes cranial sutures (adapted from Cray et al., 2010), (e) Ammonite shell (Ceratitic ammonoid) with intricate suture lines (Lin et al., 2014) (f) osteoderms of a leatherback sea turtle shell (adapted from Chen et al., 2015). (For interpretation of the references to color in this figure legend, the reader is referred to the web version of this article.)

by the deformation of nanometers-thick layers of organic materials. In addition the morphology of the interfaces plays a critical role in their mechanical response, and as seen in nacre from seashells it can act as a source of progressive locking and "geometric hardening" that delays strain localization and spreads non-elastic deformations over large volumes of materials (Fratzl et al., 2016). In natural suture lines, the interfaces have complex geometries and re-entrant features, as observed in the beak of woodpeckers (Lee et al., 2014) (Fig. 1a), the linking girdles of diatoms (Fig. 1b) (Lin et al., 2014b), the armor of threespine stickleback fishes (Song et al., 2010) (Fig. 1c), the cranial bone (Miura et al., 2009; Moazen et al., 2009) (Fig. 1d), the ammonites shells (Dunlop et al., 2011) (Fig. 1e) or turtle shells (Dunlop et al., 2011; Achrai et al., 2014) (Fig. 1f). In these examples the suture lines can channel large deformations, damp shocks and vibrations or absorb impact energy (Saunders et al., 1999). The suture lines vary in geometry and complexity across species (Allen, 2007, Maloul et al., 2014, Miura et al., 2009), and include straight suture lines as observed in new born human skull (Miura et al., 2009), triangular or wavy sutures with re-entrant features as seen in woodpecker beak (Lee et al., 2014), interlocked shapes as seen in diatoms (Genkal and Popovskaya, 2008; Manoylov et al., 2009) and ammonite shells (Lin et al., 2014a) (Fig. 1). The mechanical strength and toughness of the suture lines are largely governed by their morphology. For example, brittle sinusoidal sutures can be up to three times tougher than straight interfaces made of the same bonding material (Zavattieri et al., 2008; Cordisco et al., 2016). In ductile materials, the positioning of second phase particles into a sinusoidal pattern can guide the cracks into “pre-engineered” paths that increase toughness by a factor of 2-3 compared with the same material with random distribution of particles (Srivastava et al., 2017). Stress analysis also revealed that periodic triangular sutures homogenize the transfer of stress across the interface, which is beneficial to overall structural performance (Lin et al., 2014a, b). Recent studies have also shown that increasing the number of hierarchies within the triangulated sutures, as seen in ammonites, can augment their mechanical properties (Li et al., 2012; Li et al., 2013). The concept of sutures with tailored geometries and locking features were recently demonstrated in glasses and ceramics, which resulted in large deformations, energy absorption and enhanced toughness in otherwise all-brittle materials (Mirkhalaf et al., 2014; Malik and Barthelat, 2016). While these materials demonstrated the potential of architecture and sutures as weaker interfaces to enhance the overall mechanical performance, models and optimization approaches are yet to be developed in order to get the most of this strategy. The stiffness, strength and toughness of sutured materials were captured in models using either only elasticity and small deformations (Achrai et al., 2014; Li et al., 2012; Li et al., 2013) or elastic-plastic models (Cordisco et al., 2016), but the mechanisms and stresses associated with large pulling displacements and nonlinear geometrical locking behaviors are not well understood. Here we propose a set of models and experiments to characterize the full pullout response of a jigsaw-like suture based on frictional contact and elasticity. We first present an analytical model based on linear elasticity and frictional contact, which we compared with finite element models. A strategy to optimize the suture is then proposed based on the models. The modeling and optimization are finally verified using 3D printing and mechanical testing.

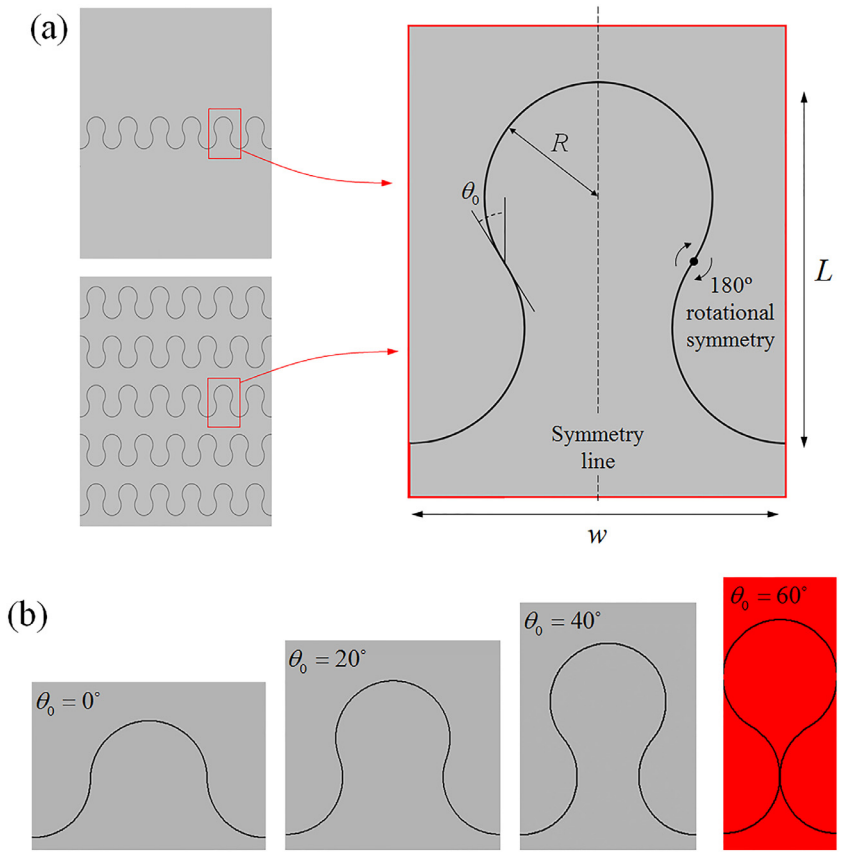

Fig. 2. (a) An individual suture with jigsaw locking features, and a material containing multiple sutures in series. The geometry and mechanics of these systems can be captured by the unit cell shown; (b) the "strength" of the geometrical interlocking is governed by the interlocking angle θ_0, where $\theta_0 < 60°$ to prevent the re-entrant regions of the tabs to intersect (case highlighted in red). (For interpretation of the references to color in this figure legend, the reader is referred to the web version of this article.)

2. Overview of the "jigsaw" suture

The sutured interfaces we considered in this work have reentrant rounded features, forming interlocks similar to a jigsaw puzzle (Fig. 2). The geometry was built from arcs of circles of radius R, and blended at locations defined by an interlocking angle θ_0. Rounded features were used to minimize stress concentrations in the solid. The patterns are periodic along the suture so that the geometry can be captured with the unit cell shown on Fig. 2a. We only considered sutures which are symmetric about a vertical axis, and which also display a 180° rotational symmetry, so that upper and lower solid parts of the suture are identical (Fig. 2a). The geometry of the suture has therefore only two independent parameters R and θ_0. It is however useful to also write the length L and the width w of the tab (Fig. 2a):

$$L = 2R(1 + \sin\theta_0) \tag{1}$$

$$w = 4R\cos\theta_0 \tag{2}$$

The interlocking angle θ_0 clearly governs the level of geometrical interlocking of the tabs (Fig. 2b). Only the cases where $\theta_0 > 0°$ generate geometrical interlocking. In addition, the contours of the tabs were not allowed to intersect, leading to the geometrical constraint $\theta_0 < 60°$. Fig. 2b shows how the level of interlocking increases when θ_0 is increased up to $\theta_0 = 60°$ which corresponds to the extreme case where the re-entrant regions of the suture intersect tangentially.

3. Analytical model of pullout response

In this work we focused on the pullout behavior of the suture, where the suture is pulled along the axis of the tabs (along the vertical direction on Fig. 2). The solid part of the suture was assumed to be isotropic and linear elastic (modulus E and Poisson's ratio ν). We also only considered the cases where the cohesion of the suture is generated by geometric interlocking and friction, with no adhesive at the interfaces. The pullout mechanism associated with the suture can therefore

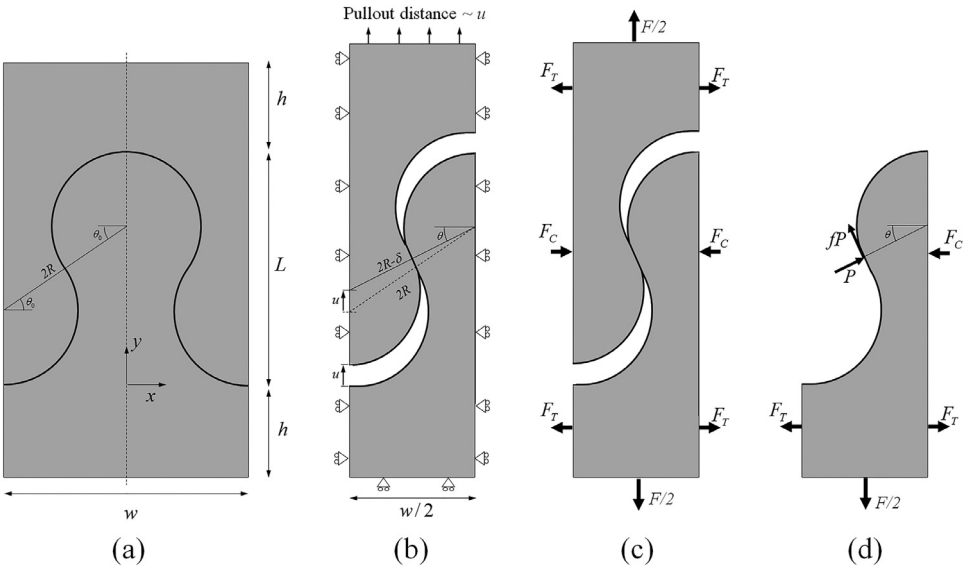

Fig. 3. (a) Representative volume element of the initial geometry for the jigsaw tab; (b) the same model with symmetry and boundary conditions applied. (c) free body diagram of the unit cell; (d) free body diagram of the lower tab only, exposing the normal and frictional forces transmitted at the contact between the tabs.

be captured using linear elasticity and frictional contact mechanics. A representative volume element of a suture in a thin plate of thickness t is shown on Fig. 3a with the key dimensions: tab radius R, interlocking angle θ_0, length L and width of the tab w, height of the upper and lower solid domains h. We assumed a thin plate, so plane stress conditions are used (the model can easily be transposed to plane strain). The suture was subjected to a uniform pull by imposing:

$$\begin{cases} u_y(x,-h)=0 \\ u_y(x,L+h)=u \end{cases} \tag{3}$$

The left and right boundaries were subjected to the periodic boundary conditions:

$$\begin{cases} u_x(w/2,y)-u_x(-w/2,y)=w\bar{\varepsilon}_x \\ u_y(w/2,y)=u_y(-w/2,y) \end{cases} \tag{4}$$

Where $\bar{\varepsilon}_x$ is the average strain in the x (transverse) direction. The geometry and the loading conditions are symmetric about axis y (Fig. 3a) and therefore the displacements must also satisfy:

$$u_x(x,y)=-u_x(-x,y) \tag{5}$$

Combining Eqs. (4) and (5) gives the periodic-symmetric boundary conditions:

$$\begin{cases} u_x(0,y)=0 \\ u_x\left(\frac{w}{2},y\right)=\frac{w}{2}\bar{\varepsilon}_x \end{cases} \tag{6}$$

We now note that $\bar{\varepsilon}_x \neq 0$ would involve elastic deformations in the two solid domains above and below the suture, with uniform strains sufficiently far from the jigsaw tab. However if h is sufficiently large, the stiffness of the solid regions along the transverse direction is high enough so that no deformation can occur in the transverse direction, $\bar{\varepsilon}_x = 0$. The boundary conditions then simply become:

$$\begin{cases} u_x(0,y)=0 \\ u_x(w/2,y)=0 \end{cases} \tag{7}$$

Fig. 3b shows the model after symmetry was applied, with the boundary conditions corresponding to Eqs. (3) and (7). This simplified geometry was used to characterize the kinematics and equilibrium of the suture. Assuming that the elastic deformations are negligible compared to the displacement generated by sliding at the interfaces and pullout, the comparison of the initial and deformed configurations yields the kinematic relations:

$$(2R-\delta)\cos\theta = 2R\cos\theta_0 \tag{8}$$

$$u = 2R\sin\theta_0 - (2R-\delta)\sin\theta \tag{9}$$

In these expressions θ is the angle of the line intersecting the centers of the two circular tabs and δ is the interference between the two tabs, which corresponds to the change of distance between the centers of the two tabs. Initially equal to *2R*, that distance becomes *2R-δ* as the tabs are pulled apart (Fig. 3b). The interference δ must be accommodated by local deformations of the tabs, which are governed by contact mechanics. In this context, δ represents the relative "approach" between the two rounded features of the tabs. The kinematics of the system is then fully characterized by the angle θ. During pullout θ decreases monotonically from $+\theta_0$ (initial configuration) down to $-\theta_0$ (the tabs lose contact). The geometric interference δ generates a contact force which results in the pullout force along the (vertical) axis of the tab, but also to (horizontal) compressive forces F_C in the tabs region on both left and right sides of the model. These compressive forces are balanced by tensile forces F_T on the left and right hand sides of the model, so that the sum of forces acting on the right hand side of the model is zero ($F_C = 2F_T$, Fig. 3c). Fig. 3d shows a free body diagram of the lower tab only, which exposes the contact forces decomposed as a normal force P and a frictional force fP acting against the direction of the pull. Balancing these forces along the vertical direction gives the pullout force F:

$$F = 2P(\sin\theta + f\cos\theta) \tag{10}$$

The forces transmitted between the two tabs are determined from the solution for the contact between two identical disks. The solution of this non-Hertzian contact mechanics problem provides the approach δ (corresponding to the interference defined above and shown in Fig. 3b) as (Johnson, 1987):

$$\delta = \frac{a^2}{2R}\left[2\ln\left(\frac{4R}{a}\right) - 1\right] \tag{11}$$

Where a is the half width of the contact surface which in plane stress is given by:

$$a^2 = \frac{4PR}{\pi tE} \tag{12}$$

where t is the thickness of the tab and E is the elastic modulus of the solid material. Eqs. (8)–(12) form a set of equations which can be solved to determine the pullout force F as function of the pullout distance u, for different parameters R, θ_0 and E. The angle θ is used as a kinematic parameter which evolves from $+\theta_0$ to $-\theta_0$ during pullout. The non-dimensional interference is first determined from Eq. (8):

$$\frac{\delta}{R} = 2\left(1 - \frac{\cos\theta_0}{\cos\theta}\right) \tag{13}$$

This expression is then combined with Eq. (9) to obtain the non-dimensional pullout distance:

$$\frac{u}{L} = \frac{\sin\theta_0 - \cos\theta_0\tan\theta}{1 + \sin\theta_0} \tag{14}$$

Here the opening u is normalized by the length of the tab L in order to get a measure of the global tensile strain in the tab generated by pullout. Meanwhile, the non-dimensional interference can be used in combination with the contact Eqs. (11) and (12) to give:

$$\frac{\delta}{R} = \frac{2}{\pi}\frac{P}{RtE}\left[\ln\left(4\pi\frac{RtE}{P}\right) - 1\right] \tag{15}$$

This equation can be solved numerically to provide a non-dimensional contact force $\frac{P}{RtE}$, which can then be used to determine the non-dimensional pullout force, using Eq. (10):

$$\frac{F}{RtE} = \frac{2P}{RtE}(\sin\theta + f\cos\theta) \tag{16}$$

However, here we prefer to use $\frac{F}{wtE}$, which provides a direct measure of the average tensile stress applied on the suture where w is the width of the tab Eq. (2) and Fig. 2a) and t is the thickness of the tab (wt is therefore the cross-sectional area of the tab). Combining Eqs. (2) and ((16) gives:

$$\frac{F}{wtE} = \frac{P}{RtE}\left(\frac{\sin\theta + f\cos\theta}{2\cos\theta_0}\right) \tag{17}$$

Fig. 4 shows a set of typical pullout responses obtained from this model. The pullout force-displacement curve for the case with no friction ($f=0$) has a sinusoidal shape where the pullout force increases up to a maximum value, and then decreases again to zero at $\theta=0$. At this particular point the interference δ and the normal contact force P are maximum, but since P acts along the direction transverse to the pull, this force does not generate any axial pullout force. Beyond this point, the contact force P is acting along the direction of pullout, and the tabs "push" on one another. At this stage F therefore becomes compressive to maintain equilibrium. The pullout force F eventually completely vanishes when the tabs lose contact, at $\theta = -\theta_0$, corresponding to $\frac{u}{L} = \frac{2\sin\theta_0}{1+\sin\theta_0}$. In the cases where $f>0$, the additional frictional contact force fP continuously resists pullout, which translates into a tensile pullout force even beyond $\theta=0$ (Fig. 4). Eq. (16) indicates that if $f > \tan\theta_0$, the pullout force F is positive throughout the entire pullout process.

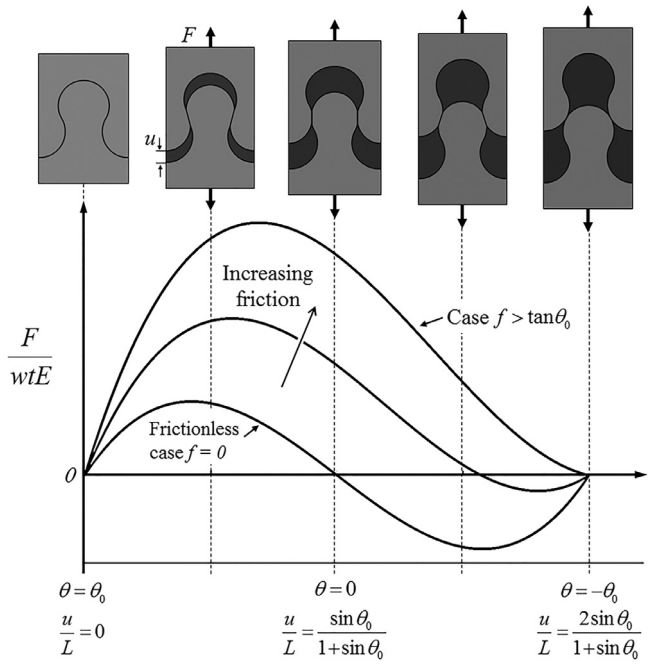

Fig. 4. Typical traction separation curves obtained from the analytical pullout model using three different friction coefficients. The deformed shape of the system is also showed at five different stages, from initial configuration to complete pullout.

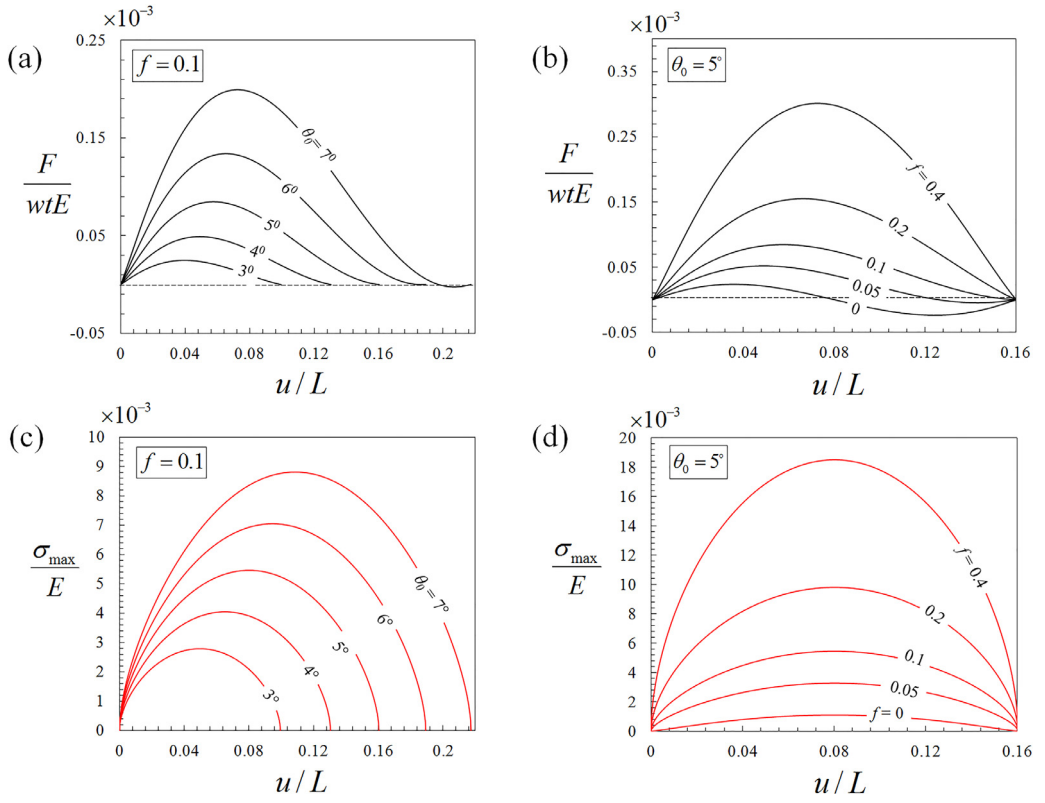

Fig. 5. Effects of (a) interlocking angle θ_0 and (b) friction f on the pullout response of the suture; effects of (c) interlocking angle θ_0 and (d) friction f on maximum tensile stress in the solid tabs.

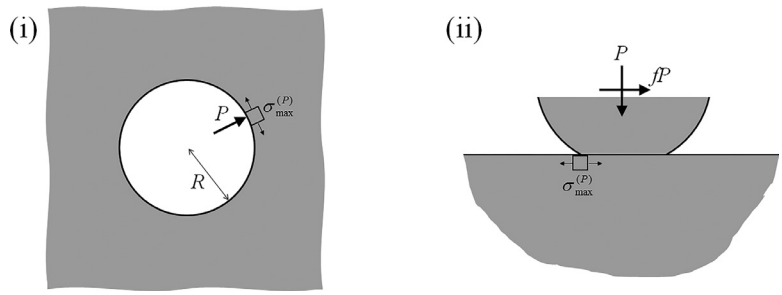

Fig. 6. The two configurations used to derive the maximum stress in the tabs: (i) point force P applied radially on the inner edge of a hole in an infinite plate; (ii) sliding disk on a half space (normal force $=P$, frictional force$=fP$). In both cases, the location of the maximum tensile stress is shown. These two solutions are superimposed to obtain the maximum stress in the solid part of the tabs.

Fig. 5a and b show the effects of the interlocking angle θ_0, and friction coefficient f on the pullout response of the suture. We first note that the pullout force is proportional to the modulus of the bulk material E, because the entire process is governed by elastic deformations in the contact region. Higher interlocking angles θ_0 increase the strength because of increased geometrical interlocking, and also increase the maximum pullout distance because the tabs stay in contact over a longer pullout distance (Eq. (14)). Higher coefficients of friction f increase the strength because of increased friction at the contact point, but do not change the maximum pullout distance, which is governed by geometry only. The friction coefficient f and interlocking angle θ_0 have therefore positive effects on the strength and energy absorption. These parameters cannot however be increased indefinitely because the high stresses in the solid parts may fracture the tab, prematurely ending the pullout process. This detrimental failure mode is considered in the next section of the analysis.

In this work we focus on the case where the tabs are made of a brittle material, so that failure of the solid tabs may be predicted by monitoring the maximum principal stress in the tabs. The maximum tensile stress in the tabs was estimated by combining two solutions: (i) a hole in an infinite plate loaded by a point force (Fig. 6i), and (ii) frictional contact mechanics (Fig. 6ii). In both cases, the maximum tensile stress occurs at the surface of the solid (in the direction tangential to the surface), and at the trailing edge of the contact between the sliding tabs.

(i) Hole in an infinite plate loaded by a frictionless pin in the in-plane direction (Ciavarella and Decuzzi, 2001; Persson, 1964): in this configuration the inner side of a hole is loaded by a contact force acting along the radial direction (Fig. 6i). The resulting maximum tensile stress is the tangential stress at the edge of the contact area. If the contact area is small ($a << R$) then the stress is given by (Ciavarella and Decuzzi, 2001; Persson, 1964):

$$\sigma_{\max}^{(P)} = \frac{P}{Rt}\frac{5-\nu}{2\pi} \tag{18}$$

where ν is the Poisson's ratio of the solid material. The stress is simply proportional to the contact force P. We note that if $R \to +\infty$ (which corresponds to the case of a point force applied in the normal direction on the surface of a half-space), one recovers $\sigma_{\max}^{(P)} \to 0$.

(ii) Sliding frictional contact: If $f>0$, the sliding of the tab generates frictional forces and shear tractions acting on the contact area. These surface tractions generate tensile stresses which are maximum at the trailing edge of the sliding contact. Assuming that the contact area is small ($a<<R$) the effect of surface curvature can be neglected and the maximum tangential stress is (Johnson, 1987):

$$\sigma_{\max}^{(fP)} = \frac{4Pf}{\pi ta} \tag{19}$$

Superposition of these two solutions gives the total stress at the trailing edge of the contact:

$$\sigma_{\max} = \sigma_{\max}^{(P)} + \sigma_{\max}^{(fP)} = \frac{P}{Rt}\frac{5-\nu}{2\pi} + \frac{4Pf}{\pi ta} \tag{20}$$

Or, after normalization:

$$\frac{\sigma_{\max}}{E} = \frac{1}{2\pi}\frac{P}{RtE}\left[(5-\nu) + 8\frac{R}{a}f\right] \tag{21}$$

Note that the stress is always highest at the edge of the contact region, even for $f=0$. The tensile stress at the root of the tab (at the smallest cross section) was always smaller than contact stresses. Fig. 5c and d shows the maximum stress as function of normalized pullout distance. The maximum stress is always positive, even if the pullout force F becomes negative. This can be explained by Eq. (21), which shows that $\sigma_{\max}$ is proportional to the normal contact force P, which is always positive. As expected, the maximum stress increases with interlocking angle and friction (Fig. 5c,d), and these

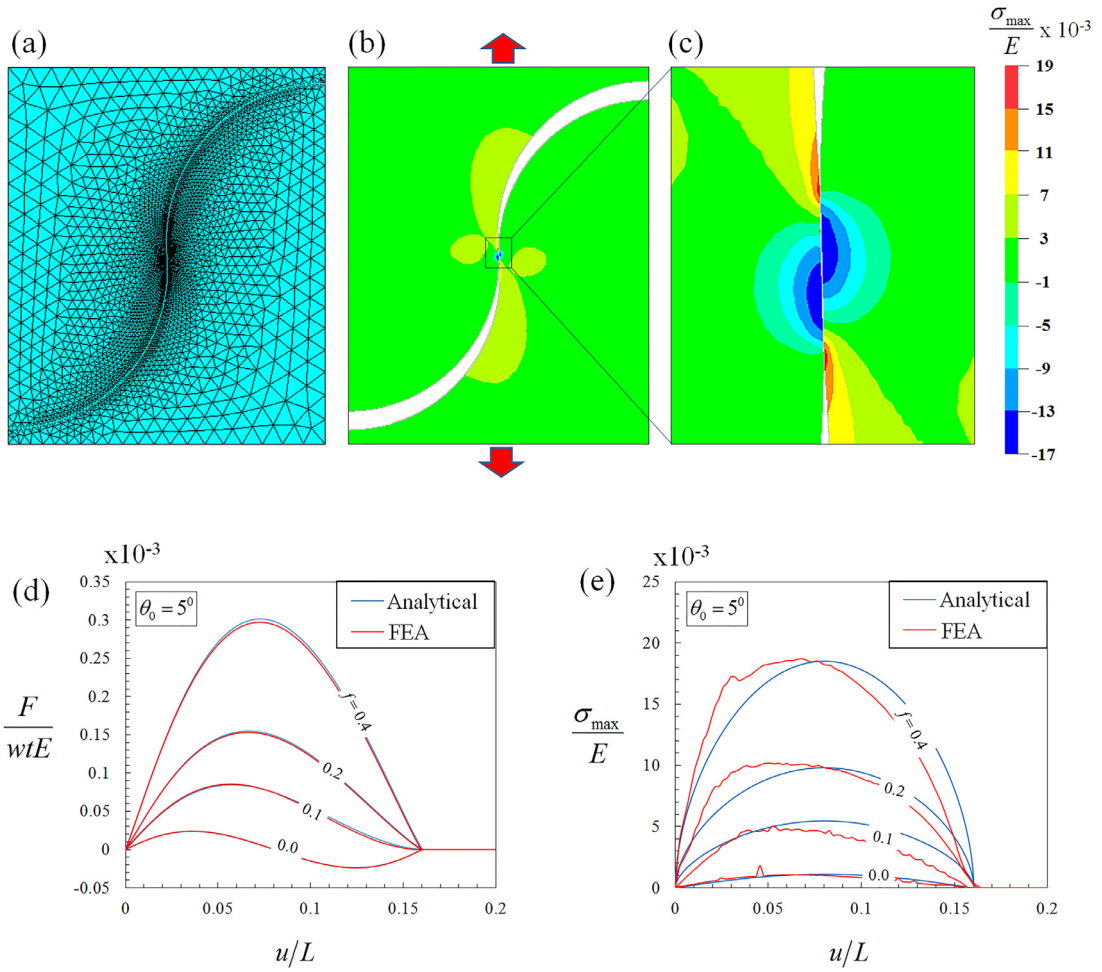

Fig. 7. (a) An example of a meshed finite element model of the jigsaw tabs ($\theta_0 = 5°$); (b) and (c) contour plots of maximum principal stress for $\theta_0 = 5°$ and $f = 0.4$; (d) and (e) traction and stresses as function of pullout distance showing a good agreement between the analytical and finite elements results.

stresses can be up to 60 times higher than the pullout traction $\frac{F}{wtE}$. The solutions also show that frictional stresses (second term in Eq. (21)) largely govern the maximum stresses in the tab. Frictional stresses are therefore the main limiting factor for the design of the tabs. Design and optimization are examined in more details in section V.

4. Finite elements simulations

In this section, we present finite element simulations for the pullout of the tabs. The objectives were to assess the validity of key assumptions in the analytical model, and to develop a platform which may be used for more complex sutures where analytical solutions may not be possible. Matlab (R2016a, MA, US) was used to automatically generate APDL input files for ANSYS (version 15.0, PA, US) (ANSYS 2013) from the parameters f and θ_0 ($R = 1$ for all simulations). The bulk of the material was meshed with quadratic, plane stress element (PLANE 183), and contact elements (CONTA 172, TARGE 169, symmetric contact) were used to simulate sliding and frictional contact at the interface. The mesh was refined to an element size of $R/5000$ near the interfaces to ensure converged, mesh independent results. Fig. 7a shows a typical finite element mesh for the jigsaw geometry. The simulations were performed in about 400 time steps (checked for convergence) and the results were post-processed automatically using ANSYS ADPL and Matlab. This procedure was used to automatically run models (Barthelat and Mirkhalaf, 2013) for 80 combinations of θ_0 and f. Fig. 7d and e are representative comparisons which show excellent agreement between the finite elements and analytical predictions in terms of pullout response and maximum tensile stress within the material. The maximum stress from the finite element model also always occurred at the edge of the contact region (Fig. 7b and c), in accordance with the predictions form the analytical solution. Finite elements and analytical solutions are both subjected to approximations and therefore neither of these models are exact solutions that could be used for validation. However, the fact that both models agree to a large extent suggests that they can capture the response of the system with an acceptable level of accuracy. For the case of the simple jigsaw geometry considered here,

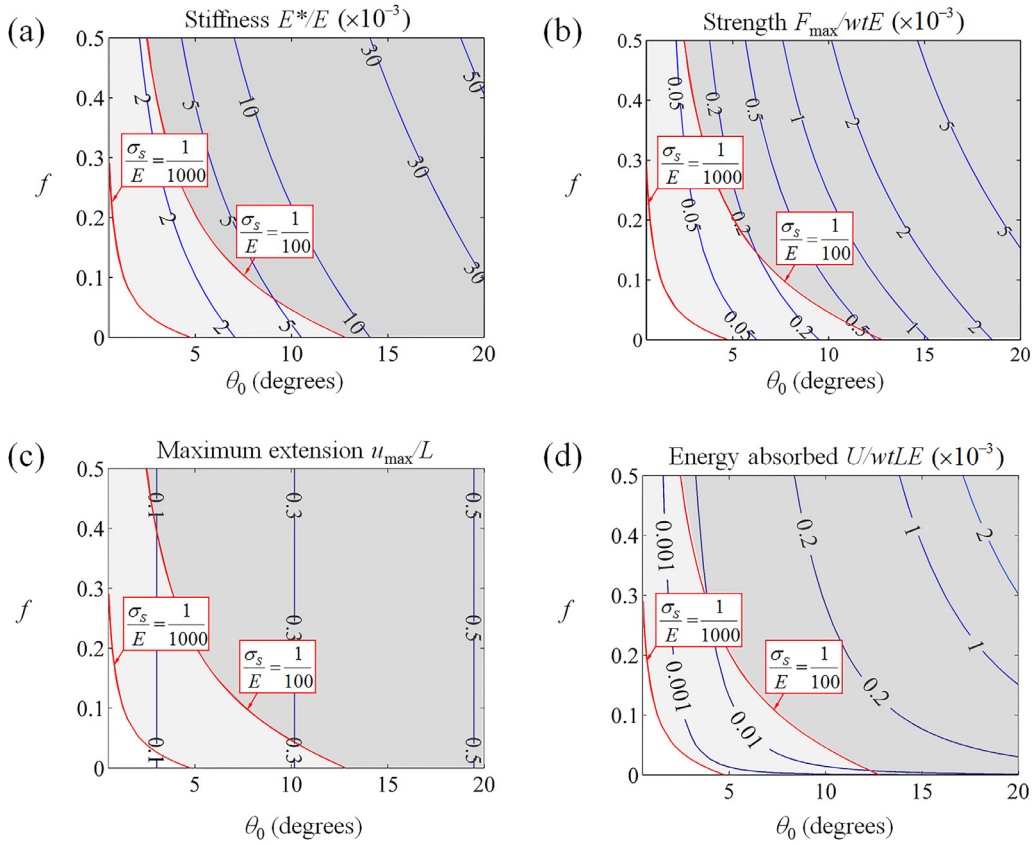

Fig. 8. Mechanical properties of the jigsaw suture as function of interlocking angle θ_0 and friction coefficient f. The properties are plotted as blue contour lines on each of the diagrams. (a) stiffness; (b) strength; (c) maximum extension and (d) energy absorbed. In each case the red lines show limit designs for which the tensile strength of the material is reached ($\sigma_s/E=1/100$ and $\sigma_s/E=1/1000$). (For interpretation of the references to color in this figure legend, the reader is referred to the web version of this article.)

the analytical solution is easier and faster to implement and use, and therefore it was used for the design optimization presented in the next section.

5. Design optimization

The models developed for pullout showed that increasing either θ_0 or f improves the pullout response of jigsaw tab, but also gives rise to tensile stresses in the solid material which can fracture the tabs. This failure mode is considered detrimental since it prematurely interrupts the dissipative mechanisms at the interfaces. Here we performed an optimization approach based on exhaustive search of the design space to identify the best combination(s) of design parameters for any given set of desired of normalized stiffness, strength, maximum extension, and energy absorption. The normalized stiffness of the suture is defined as:

$$\frac{E*}{E}=L\frac{d}{du}\left(\frac{F}{wtE}\right)_{u=0} \tag{22}$$

The strength is simply $\frac{F_{max}}{wtE}$, the maximum elongation is $\frac{u_{max}}{L}$ and the energy absorbed is given by the area under the pullout force-displacement curve:

$$\frac{U}{wtLE}=\int_0^{u_{max}}\frac{F}{wtE}\frac{du}{L} \tag{23}$$

Fig. 8a–d show contour lines (the blue lines) for these four properties as functions of f and θ_0. All properties increase with f and θ_0. The frictionless case $f=0$ can generate stiffness strength through purely geometric interlocking, but it does not absorb energy. The limiting factor for the design is the fracture of the solid tabs, which is governed by the strength of the material. The tabs will therefore fracture when $\sigma_{max}=\sigma_S$, or $\frac{\sigma_{max}}{E}=\frac{\sigma_S}{E}$ where σ_{max} is the maximum tensile stress predicted from the model (Eq. (21)) and σ_S is the tensile strength of the solid material. For most engineering materials the ratio between the tensile strength and modulus is in the range of $\frac{\sigma_S}{E}=\frac{1}{1000}$ to $\frac{\sigma_S}{E}=\frac{1}{100}$ (Ashby, 2011). The contour lines for

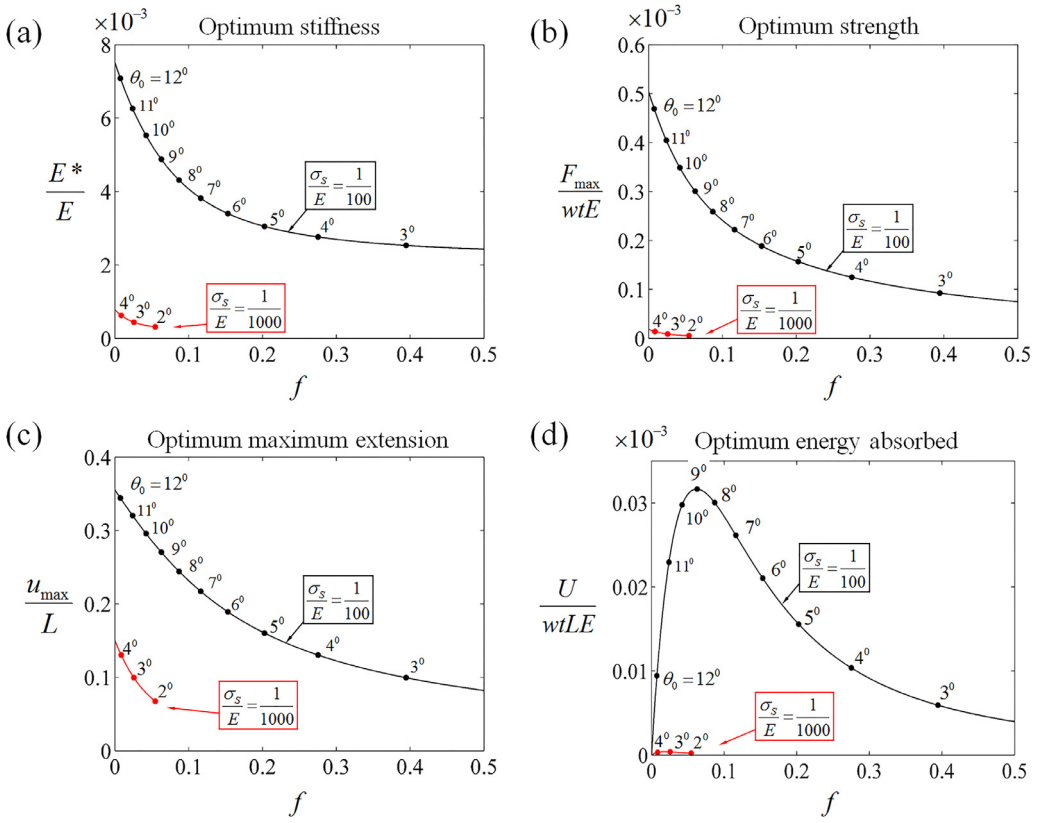

Fig. 9. Optimum parameters and mechanical properties for the limiting tensile strength of the bulk material for $\sigma_s/E = 1/100$ and $\sigma_s/E = 1/1000$: (a) optimum stiffness; (b) optimum strength; (c) optimum maximum extension and (d) optimum energy absorbed.

$\frac{\sigma_{max}}{E} = \frac{1}{1000}$ and $\frac{\sigma_{max}}{E} = \frac{1}{100}$ are therefore superimposed in red on Fig. 8a–d. These lines define the boundaries of gray areas in the upper right portion of the diagram, and any combination of f and θ_0 in the greyed areas of these diagrams leads to the brittle fracture of the tabs. The optimum designs in terms of f and θ_0 will make the most of the solid material and will lie one of the red lines corresponding to the $\frac{\sigma_S}{E}$ ratio for the material considered. These diagrams can therefore be used to identify the optimum suture properties that can be achieved by simply intersecting the contour lines of properties with the limiting lines for tab fracture. For example, if the friction at the interface is $f = 0.15$ and the material of the tabs is relatively strong ($\frac{\sigma_S}{E} = \frac{1}{100}$), the point where the horizontal line $f = 0.15$ and the contour line $\frac{\sigma_S}{E} = \frac{1}{100}$ intersect gives the optimum interlocking angle of about $\theta_0 = 7°$. In Fig. 8b that point corresponds to an optimum suture strength or about $\frac{F_{max}}{wtE} = 0.2 \times 10^{-3}$. The coordinates of these intercepts was collected for all values of f, with the results displayed on Fig. 9. These plots can serve as guidelines for optimization: with a given friction coefficient f, the optimum stiffness, strength, elongation and energy absorption can be easily identified, along with the interlocking angle θ_0 that will achieve this optimized property. For example, for relatively weak and stiff materials such as ceramics and glasses ($\sigma_s/E = 1/1000$), the value of interlocking angles and friction coefficients that will prevent tab fracture are small and cover a narrow range ($\theta_0 = 2°–4°$ and $f = 0–0.05$). For stronger and/or more compliant materials such as metals and polymers ($\sigma_s/E = 1/100$), the range of interlocking angles and friction coefficients that will prevent tab fracture is much wider ($\theta_0 = 2°–12°$ and $f = 0–0.5$). The optimization results also reveals a counterintuitive but important guideline. Parametric studies show that higher coefficient of friction can promote strength, stiffness and energy absorption. However, the high frictional stresses at the interface also generate large tensile stresses in the contact areas, which can precipitate the fracture of the tabs. In contrast, low friction coefficients minimize the tensile stresses in the contact regions, making it possible to use higher interlocking angles without fracturing the tabs, which in turn generate high stiffness and strength. Interestingly, the optimization results show that the maximum stiffness (Fig. 9a), strength (Fig. 9b) and extension (Fig. 9c) are actually achieved for $f = 0$ and high interlocking angle ($\theta_0 \sim 13°$ for $\sigma_s/E = 1/100$). This result does not however apply to energy dissipation because friction at the interfaces is the only dissipative mechanism in the system. Zero friction $f = 0$ leads to $U = 0$, which is undesirable for the toughness of the suture. The trend in terms of energy is more complex and displays an optimum coefficient of friction which is function of the ratio σ_s/E only. The models give an optimum friction coefficient for energy absorption of $f = 0.080$ for $\sigma_s/E = 1/100$ and $f = 0.018$ for $\sigma_s/E = 1/1000$. These friction coefficients are relatively small, but again for these optimized cases the frictional energy dissipated at the interface can be magnified by high interlocking angles.

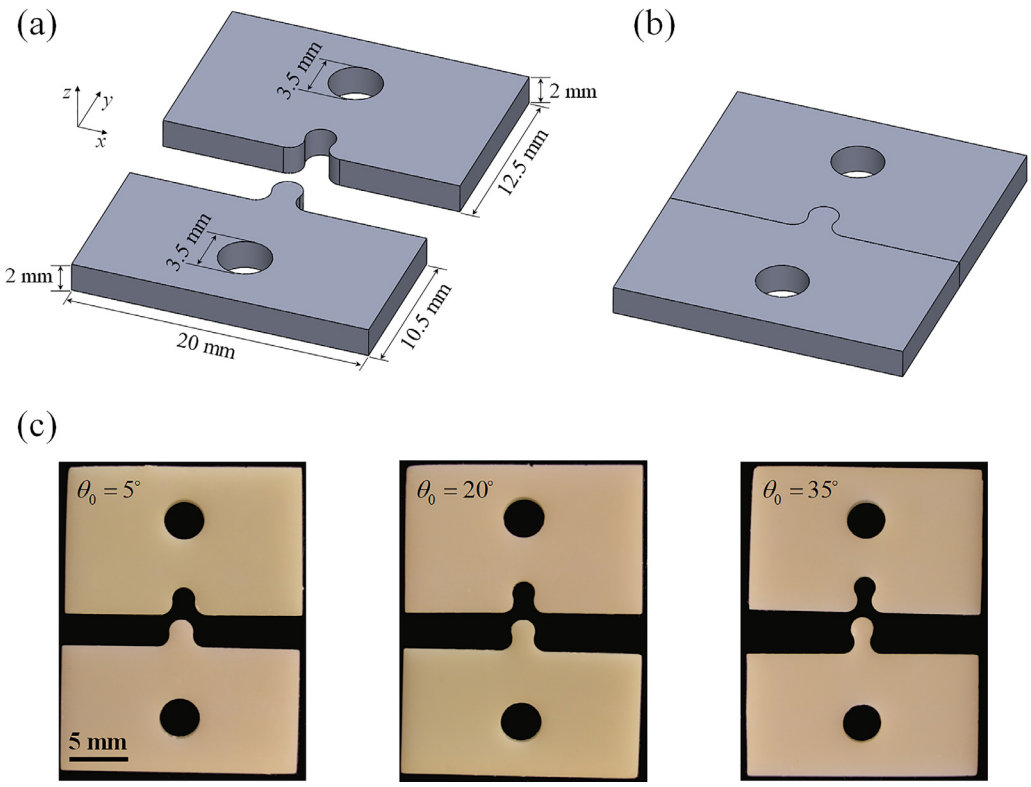

Fig. 10. 3D printed suture samples: diagrams showing (a) the shape and dimensions of the two parts of the samples and (b) the assembled sample; (c) pictures of samples with different interlocking angles, before assembly.

6. 3D printing and mechanical testing

In order to validate the pullout models and to explore the optimum designs suggested above, we fabricated and tested jigsaw like interlocked sutures using 3D printing and miniaturized mechanical testing. The solid material was Acrylonitrile Butadiene Styrene (ABS) (EnvisionTech Perfactory, MI, US). A high resolution 3D printer (Micro HiRes Machine, EnvisionTech) based on the digital light processing (DLP) technology (Studart, 2016; Tumbleston et al., 2015) was used for fabrication. This particular 3D printer produces fully dense, isotropic solid components with a high level of geometrical fidelity and very smooth surfaces. We measured the mechanical properties of the as-printed ABS material using a three-point bending configuration ($N=3$), and found a modulus $E=1.7\pm0.2$ GPa, and a strength $\sigma_S=118\pm12$ MPa (failure was brittle). We verified that the material is isotropic by performing the same measurement along three different orientations with respect to the direction of printing. We also measured the kinetic coefficient of friction of ABS on ABS using ASTM D1894 (American Society for Testing and Materials 1894), revealing a coefficient of friction $f=0.35\pm0.04$ ($N=3$) for this material. Jigsaw-like sutures consisting of a single tab with different interlocking angles $\theta_0=5°$, 10°, 15°, 20°, with $R=1$ mm and thickness $t=2$ mm (Fig. 10a) were 3D printed. The printing direction was along the out-of-plane direction for the tabs (axis z on Fig. 10a) and the layer thickness was 50 μm. In order to prevent any gaps at the interface of the suture, the two solid parts of the sample were printed individually, and then assembled by sliding along the out-of-plane direction (Fig. 10b and c). Two holes were made in the samples to apply the pull-out force (Fig. 10a) through loading pins. Each sample contained a single interlocking tab, and in order to prevent lateral bending and transverse strains during pullout (which would not be representative of a periodic suture), the total width of the sample was set to about five times the width of the tab. Pictures of the actual samples with three different interlocking angles are shown in Fig. 10c. The tests were performed at a pulling rate of 0.05 mm/s and with optical imaging to measure displacements. The pullout force F was divided by the cross section wt to obtain the average stress applied onto the interlocking tab, and the pullout displacement u was normalized by the length of the locking tab L. Three samples were tested for each geometry ($N=3$) for repeatability. Fig. 11a shows the representative pullout behavior of the suture for each of the four interlocking angles. The bell shape of the curves is similar to the theoretical predictions and has the characteristics of a progressive failure (Barthelat and Mirkhalaf, 2013). The stiffness, strength, maximum elongation and energy absorption all increased with interlocking angle as predicted by the models. Sutures with interlocking angle of 20° fractured prematurely, with cracks emanating from the edges of the contact region (Fig. 11a), also in agreement with the stress analysis presented above. We compared the experimental pullout response for interlocking angles $\theta_0=5°$, 10°, 15°, 20° with the prediction of the models using the values $E=1.72$ GPa and $f=0.35$ measured experi-

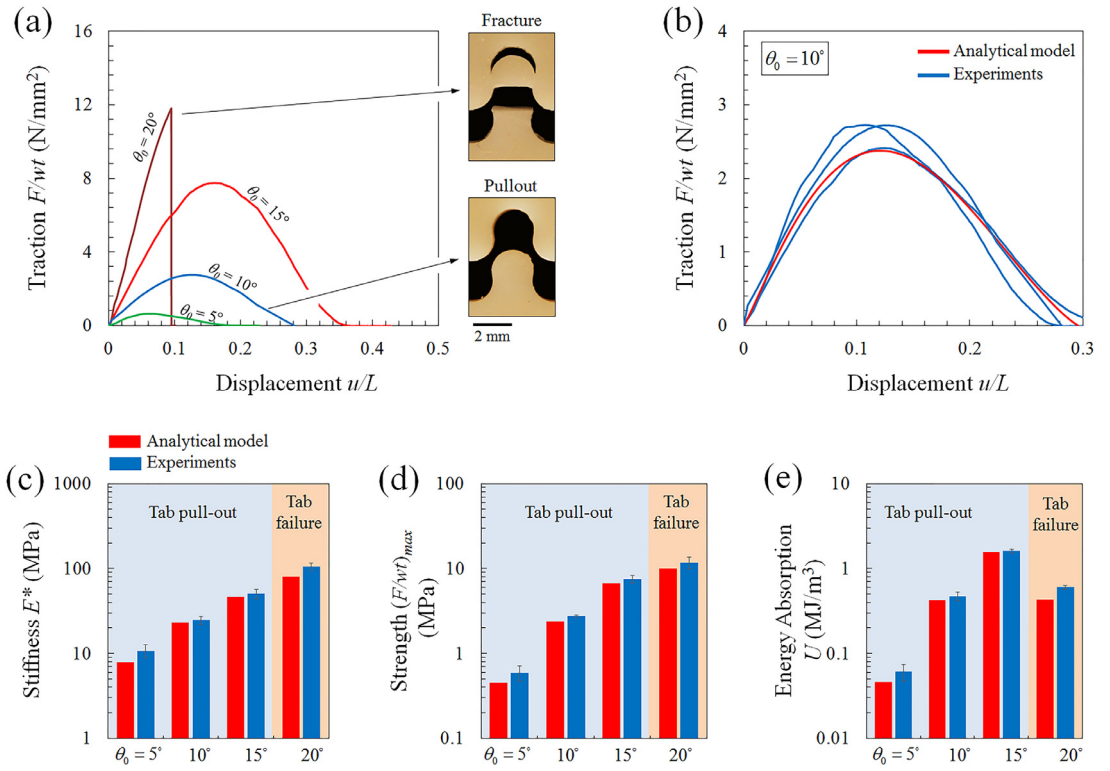

Fig. 11. Experiments on the jigsaw interlocked tabs. (a) representative pullout curves with different interlocking angles ($\theta_0 = 5°$, 10°, 15°, 20°), with representative pictures showing two different failure modes: tab pullout and fracture. (b) comparison between simulation and experimental pullout curves for sutures with $\theta_0 = 10°$. (c) stiffness, (d) strength, and (e) energy absorption of the suture as a function of interlocking angle, with comparisons from models (the error bars represent ± one standard deviation of the variable).

mentally for ABS. Experiments and models agreed well, Fig. 11b showing a representative comparison obtained for the case $\theta_0 = 10°$. Figs. 11c–e summarize the experimental properties of the suture and show how the stiffness, strength and energy absorption increase with θ_0, up to $\theta_0 = 15°$. The model could capture the experimental values for each property over one order of magnitude. On a logarithmic scales with a reference of 0.001 for the lower bound, the difference between model and experiment was only 0.3–7% (Fig. 11c–e). On a linear scale the difference is larger and in the 5–25% range. The model could therefore capture the experimental values relatively well for all properties. The tabs fractured at an interlocking angle of 20°, which can also be compared with our models using $E = 1.72$ GPa, $f = 0.35$, Poisson's ratio $\nu = 0.4$ (typical value for rigid polymers (Tschoegl et al., 2002)), and $\sigma_s = 118$ MPa corresponding to $\frac{\sigma_S}{E} \approx 0.07$. Using these values, our model predicted that the tab would fractured for interlocking angles $\theta_0 > 14.66°$. In the experiments the tabs were intact for $\theta_0 = 15°$ but fractured for $\theta_0 = 20°$ the model therefore only slightly underestimated the strength of the tab. We did not observe permanent, plastic deformations in the tabs, which is consistent with a yielding model based Johnson (1987) for frictional contact problems. Using Von-Mises yield criteria, the model predicts an onset of yielding at a maximum contact pressure of $(p_0)_y = 0.8\sqrt{3}\sigma_y$ for a friction coefficient of $f = 0.35$. With a 0.2% offset yield strength of ABS of $\sigma_y = 109.8 \pm 8.7$ MPa measured experimentally, the model predicts an onset of yielding at $(p_0)_y = 152.2$ MPa. The maximum contact pressure for the two identical disks is given by (Johnson, 1987):

$$p_0 = \frac{2P}{\pi t a} \tag{24}$$

The maximum force P occurs at the maximum interference between the tabs given by:

$$\delta_{\max} = 2R(1 - \cos\theta_0) \tag{25}$$

By solving Eqs. (11), (12), (24) and (25) numerically, we determined that the tabs start to yield at interlocking angle $\theta_0 = 16.6°$ which is more than the interlocking angle $\theta_0 = 14.7°$ at which the tabs fracture in a brittle fashion. The implication is that the state of the stresses within the tabs is such that the tabs break before they yield. This prediction agrees with the experiments: the tabs fail catastrophically with little or no plastic deformation.

The models and optimization presented in the previous sections suggest that lower coefficient of friction at the interface would increase the overall properties of the optimized tab, a seemingly counter intuitive result we wanted to verify experimentally. We reduced the coefficient of friction by using paraffin as lubricant (Jia et al., 2007) and measured $f = 0.142 \pm 0.021$

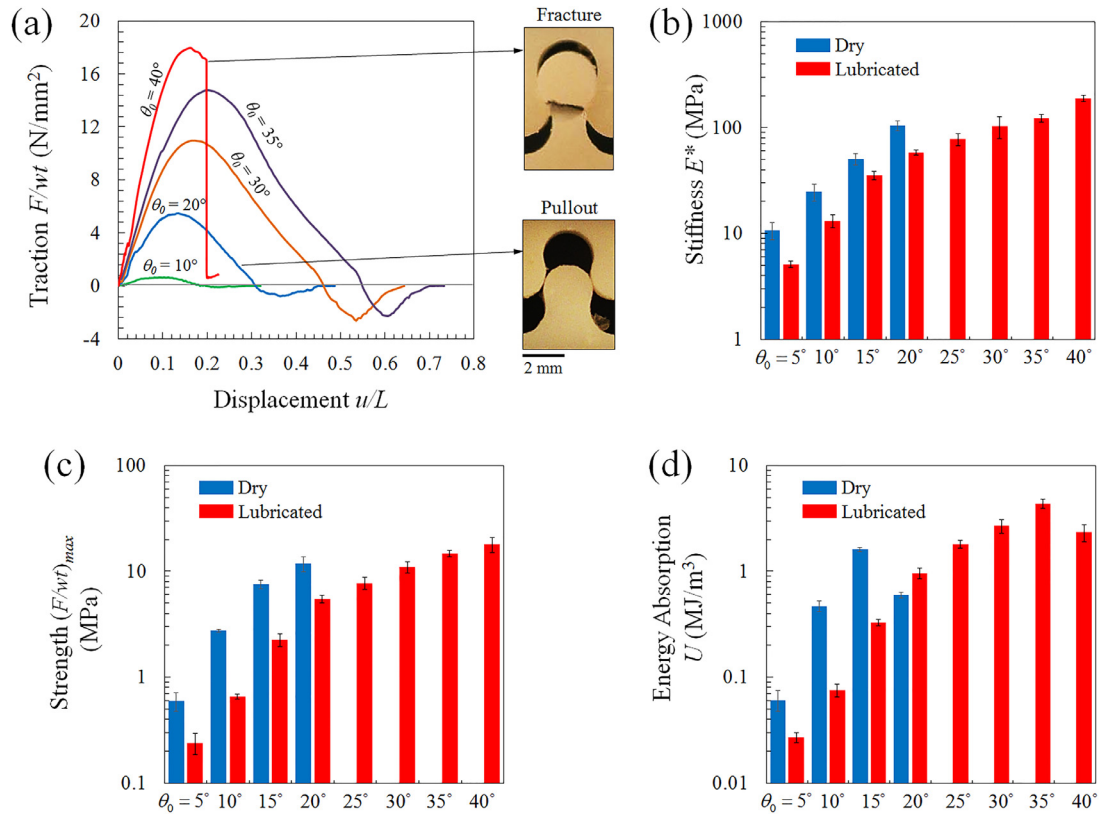

Fig. 12. Experimental results from sutures with reduced friction coefficient: (a) representative pullout behavior of the lubricated tab with different interlocking angles ($\theta_0 = 10°$, 20°, 30°, 35°, 40°) with pictures showing two different failure modes. (b) stiffness, (c) strength, and (d) energy absorption of the lubricated suture as functions of interlocking angle. Comparison between dry and lubricated cases is also shown (the error bars represent ±one standard deviation of the variable).

using a standard friction test (American Society for Testing and Materials 1894). This value of friction coefficient is about 2.5 times lower than the dry case. We fabricated a new batch of sutured materials with interlocking angles of $\theta_0 = 10°$, 20°, 30°, 35°, and 40°. Prior to assembly of the samples, a thin coating of paraffin was applied on the inner surfaces of the tabs. A set of representative experimental pullout curves are shown in Fig. 12a. With a reduced friction, the interlocking angle could be increased to $\theta_0 = 35°$ without breaking the tabs, as predicted by the model. However the model could not match the experimental curves, which we attributed to the extensive plastic deformations in the tabs (these limitations of our models would not apply when designing sutures in ceramics or glasses). Nevertheless, the experimental results (Fig. 12b,c and d) confirmed that significantly higher stiffness, strength and energy absorption can be achieved at higher interlocking angles with a lower coefficient of friction. The stiffness, strength and energy absorption of the lubricated suture with the optimum interlocking angle of $\theta_0 = 35°$, were 2.5, 2 and 2.7 times higher than the highest stiffness, strength and energy absorption achieved with the non-lubricated samples (at $\theta_0 = 15°$).

A potential application of the jigsaw-like suture exploits its energy absorption and toughness, as seen in recent examples of all-brittle architectured materials that combine surface hardness with deformability, energy absorption and impact resistance (Mirkhalaf et al., 2014, Malik and Barthelat, 2016; Mirkhalaf et al., 2016). Here we calculated the effective toughness of the sutured interface with the toughness of ABS. The fracture toughness of plain ABS was measured using a 3-point-bending fracture test configuration (Standard, 2001) and was found to be $J_S = 300 \pm 28.6\,\mathrm{J.m^{-2}}$. By interpreting the pullout data as a traction separation law which would govern the mode I fracture of the suture, the effective toughness of the suture is simply the area under the experimental traction (F/wt) separation (u) curve. Using this method we measured a toughness $J = 13.76 \pm 1.7\,\mathrm{kJ.m^{-2}}$ for the optimum suture ($\theta_0 = 35°$, lubricated), which is about 45 higher than plain ABS. Incorporating sutures is therefore a powerful method to increase the effective toughness of materials and structures.

7. Summary

Sutured materials are prominent in natural materials and they are now attracting an increasing amount of attention in the context of bio-inspired engineering applications. The strength and fracture mechanics of these sutures were characterized in the past for sinusoidal morphologies (Zavattieri et al., 2008, Cordisco et al., 2016), or more complex interlocking

morphologies but only at small strains (Achrai et al., 2014, Li et al., 2012, Li et al., 2013). In this work we proposed, for the first time, a model that captures the complete pullout of jigsaw-like features over long distances, with progressive interlocking and frictional interactions at the interfaces. The model also provides the maximum tensile stress in the solid parts of the tabs, which can be used to predict and prevent the brittle fracture of the tabs. The main conclusions from the models are as follow:

- The resistance to pull-out of the suture increases with angle θ_0 and friction coefficient f.
- The highest tensile stresses in the solid are generated by frictional tractions at the contact between the tabs, and occur at the edge of the contact area. These stresses are always significantly larger than the tensile stresses occurring in the smallest cross section of the tabs.
- The design guidelines we present here are useful for non-adhesive contact of jigsaw-like sutures in any brittle material subjected to tensile loading.
- Optimization revealed that to maximize stiffness, strength and energy absorption it is preferable to use low coefficients of friction to minimize the stresses near the frictional contact, combined with high interlocking angles to generate high structural properties for the suture.

We validated the models and these observations by 3D printing and testing actual jigsaw interlocked tabs made of ABS, a relatively brittle polymer. Good agreements between the predicted and actual pullout curves were obtained for different interlocking angles. The models also predicted the failure of tabs with a good accuracy, in terms of both the interlocking angle at which the tabs start to break and the location of the failure (trailing edge of the contact). We finally verified experimentally by lubricating the interfaces that designs with low coefficients of friction and high interlocking angles lead to higher properties overall, including higher energy dissipation. The suture interface is particularly remarkable for its toughness: we found that it is 45 times tougher than plain ABS (in J-terms). These models and optimization results therefore provide a robust platform for the design and optimization of jigsaw-like sutures, which can be exploited in compliant interfaces (Dunlop et al., 2011, Achrai et al., 2014), in morphologically enhanced bond lines (Miura et al., 2009), and in damping and shock absorbing applications (Saunders et al., 1999). Dense network of sutures in materials can lead to unusual and attractive homogenized performance which can surpass monolithic materials: enhanced toughness, deformation and energy absorption in otherwise fragile materials (Mirkhalaf et al., 2014, Malik and Barthelat, 2016). Finally, the models presented here are restricted to simple jigsaw geometries with only two geometrical parameters (curvature and interlocking angle). Enriching the shape of the suture is likely to generate a wider range of properties, for example by generating “double locking” upon pullout (Mirkhalaf and Barthelat, 2017). The models developed here can serve as a starting point for the exploration and optimization of these more complex suture morphologies.

Acknowledgments

This work was supported by Natural Sciences and Engineering Research Council of Canada and by the Fonds de Recherche du Québec – Nature et Technologies. IAM was supported by a Scholarship from the Nigerian Government through the National Universities commission.

References

Achrai, B., Bar-On, B., Wagner, H.D., 2014. Bending mechanics of the red-eared slider turtle carapace. J. Mech. Behav. Biomed. Mater. 30, 223–233.
Allen, E.G., 2007. Understanding ammonoid sutures: new insight into the dynamic evolution of Paleozoic suture morphology. In: Landman, N.H., Davis, R.A., Mapes, R.H. (Eds.), Cephalopods Present and Past: New Insights and Fresh Perspectives, pp. 159–180.
American Society for Testing and Materials, 1894. Standard Test Method for Static and Kinetic Coefficients of Friction of Plastic Film and Sheeting.
ANSYS, 2013. ANSYS® Academic Research, *Release 15.0*.
Ashby, M.F., 2011. Chapter 4 - Material property charts. In: Materials Selection in Mechanical Design. Butterworth-Heinemann, Oxford, pp. 57–96.
Bajaj, D., et al., 2010. Fracture processes and mechanisms of crack growth resistance in human enamel. Jom 62 (7), 76–82.
Barthelat, F., et al., 2007. On the mechanics of mother-of-pearl: a key feature in the material hierarchical structure. J. Mech. Phys. Solids 55 (2), 306–337.
Barthelat, F., 2015. Architectured materials in engineering and biology: fabrication, structure, mechanics and performance. Int. Mater. Rev. 60 (8), 413–430.
Barthelat, F., Mirkhalaf, M., 2013. The quest for stiff, strong and tough hybrid materials: an exhausti7ve exploration. J. R. Soc. Interface 10 (89), 20130711.
Barthelat, F., Yin, Z., Buehler, M.J., 2016. Structure and mechanics of interfaces in biological materials. Nat. Rev. Mater. 1, 16007.
Chen, I.H., Yang, W., Meyers, M.A., 2015. Leatherback sea turtle shell: a tough and flexible biological design. Acta Biomaterialia 28, 2–12.
Ciavarella, M., Decuzzi, P., 2001. The state of stress induced by the plane frictionless cylindrical contact. I. The case of elastic similarity. Int. J. Solids Struct. 38 (26–27), 4507–4523.
Cordisco, F.A., et al., 2016. Mode I fracture along adhesively bonded sinusoidal interfaces. Int. J. Solids Struct. 83, 45–64.
Cray, J., Mooney, M.P., Siegel, M.I., 2010. Timing of ectocranial suture activity in Pan troglodytes as related to cranial volume and dental eruption. Anat. Rec. 293 (8), 1289–1296.
Currey, J.D., 2002. Bones : Structure And Mechanics. Princeton University Press, Princeton, NJ.
Dunlop, J.W.C., Weinkamer, R., Fratzl, P., 2011. Artful interfaces within biological materials. Mater. Today 14 (3), 70–78.
Fratzl, P., et al., 2016. The mechanics of tessellations–bioinspired strategies for fracture resistance. Chem. Soc. Rev. 45 (2), 252–267.
Fratzl, P., Burgert, I., Gupta, H.S., 2004. On the role of interface polymers for the mechanics of natural polymeric composites. Phys. Chem. Chem. Phys. 6 (24), 5575–5579.
Genkal, S.I., Popovskaya, G.I., 2008. Centric diatom algae of the Selenga river and its delta branches. Inland Water Biol. 1 (2), 120–128.
He, M.Y., Evans, A.G., Hutchinson, J.W., 1994. Crack deflection at an interface between dissimilar elastic materials: role of residual stresses. Int. J. Solids Struct. 31 (24), 3443–3455.
Jia, B.-B., et al., 2007. Tribological behaviors of several polymer–polymer sliding combinations under dry friction and oil-lubricated conditions. Wear 262 (11), 1353–1359.

Johnson, K.L., 1987. Contact Mechanics. Cambridge University Press.
Khayer Dastjerdi, A., Rabiei, R., Barthelat, F., 2013. The weak interfaces within tough natural composites: experiments on three types of nacre. J. Mech. Behav. Biomed. Mater. 19, 50–60.
Koester, K.J., Ager III, J.W., Ritchie, R.O., 2008. The true toughness of human cortical bone measured with realistically short cracks. Nat. Mater. 7 (8), 672–677.
Lee, N., et al., 2014. Hierarchical multiscale structure-property relationships of the red-bellied woodpecker (Melanerpes carolinus) beak. J. R. Soc. Interface 11 (96).
Li, Y., Ortiz, C., Boyce, M.C., 2012. Bioinspired, mechanical, deterministic fractal model for hierarchical suture joints. Phys. Rev. E 85 (3).
Li, Y., Ortiz, C., Boyce, M.C., 2013. A generalized mechanical model for suture interfaces of arbitrary geometry. J. Mech. Phys. Solids 61 (4), 1144–1167.
Lin, E., et al., 2014a. Tunability and enhancement of mechanical behavior with additively manufactured bio-inspired hierarchical suture interfaces. J. Mater. Res. 29 (17), 1867–1875.
Lin, E., et al., 2014b. 3D printed, bio-inspired prototypes and analytical models for structured suture interfaces with geometrically-tuned deformation and failure behavior. J. Mech. Phys. Solids 73, 166–182.
Malik, I.A., Barthelat, F., 2016. Toughening of thin ceramic plates using bioinspired surface patterns. Int. J. Solids Struct.
Maloul, A., et al., 2014. Characterization of craniofacial sutures using the finite element method. J. Biomech. 47 (1), 245–252.
Manoylov, K.M., Ognjanova-Rumenova, N., Stevenson, R.J., 2009. Morphotype variations in subfossil diatom species of Aulacoseira in 24 Michigan lakes, USA. Acta Botanica Croatica 68 (2), 401–419.
Meyers, M.A., et al., 2008. Biological materials: structure and mechanical properties. Prog. Mater. Sci. 53 (1), 1–206.
Mirkhalaf, M., Barthelat, F., 2017. Design, 3D printing and testing of architectured materials with bistable interlocks. Extreme Mech. Lett. 11, 1–7.
Mirkhalaf, M., Dastjerdi, A.K., Barthelat, F., 2014. Overcoming the brittleness of glass through bio-inspiration and micro-architecture. Nat. Commun. 5, 3166.
Mirkhalaf, M., Tanguay, J., Barthelat, F., 2016. Carving 3D architectures within glass: exploring new strategies to transform the mechanics and performance of materials. Extreme Mech. Lett. 7, 104–113.
Miura, T., et al., 2009. Mechanism of skull suture maintenance and interdigitation. J. Anat. 215 (6), 642–655.
Moazen, M., et al., 2009. Assessment of the role of sutures in a lizard skull: a computer modelling study. Proc. R. Soc. B-Biol. Sci. 276 (1654), 39–46.
Persson, A., 1964. On the Stress Distribution of Cylindrical Elastic Bodies in Contact inst.
Ritchie, R.O., 2011. The conflicts between strength and toughness. Nat. Mater. 10 (11), 817–822.
Saunders, W.B., Work, D.M., Nikolaeva, S.V., 1999. Evolution of complexity in paleozoic ammonoid sutures. Science 286 (5440), 760–763.
Smith, B.L., et al., 1999. Molecular mechanistic origin of the toughness of natural adhesives, fibres and composites. Nature 399 (6738), 761–763.
Song, J., et al., 2010. Quantitative microstructural studies of the armor of the marine threespine stickleback (Gasterosteus aculeatus). J. Struct. Biol. 171 (3), 318–331.
Srivastava, A., Osovski, S., Needleman, A., 2017. Engineering the crack path by controlling the microstructure. J. Mech. Phys. Solids 100, 1–20.
Standard, A., 2001. Standard test method for measurement of fracture toughness. ASTM 1–46 E1820-01.
Studart, A.R., 2016. Additive manufacturing of biologically-inspired materials. Chem. Soc. Rev. 45 (2), 359–376.
Tschoegl, N.W., Knauss, W.G., Emri, I., 2002. Poisson's ratio in linear viscoelasticity–a critical review. Mech. Time-Depend. Mater. 6 (1), 3–51.
Tumbleston, J.R., et al., 2015. Continuous liquid interface production of 3D objects. Science 347 (6228), 1349–1352.
Zavattieri, P.D., Hector Jr., L.G., Bower, A.F., 2008. Cohesive zone simulations of crack growth along a rough interface between two elastic-plastic solids. Eng. Fract. Mech. 75 (15), 4309–4332.